



This discussion paper is/has been under review for the journal Geoscientific Model Development (GMD). Please refer to the corresponding final paper in GMD if available.

NCAR global model topography generation software for unstructured grids

P. H. Lauritzen¹, J. T. Bacmeister¹, P. F. Callaghan¹, and M. A. Taylor²

¹National Center for Atmospheric Research, 1850 Table Mesa Drive, Boulder, Colorado, USA

²Sandia National Laboratories, Albuquerque, New Mexico, USA

Received: 12 May 2015 – Accepted: 04 June 2015 – Published: 22 June 2015

Correspondence to: P. H. Lauritzen (pel@ucar.edu)

Published by Copernicus Publications on behalf of the European Geosciences Union.

GMDD

8, 4623–4651, 2015

NCAR topography
software

P. H. Lauritzen et al.

Title Page

Abstract

Introduction

Conclusions

References

Tables

Figures



Back

Close

Full Screen / Esc

Printer-friendly Version

Interactive Discussion



Abstract

It is the purpose of this paper to document the NCAR global model topography generation software for unstructured grids. Given a model grid, the software computes the fraction of the grid box covered by land, the gridbox mean elevation, and associated sub-grid scale variances commonly used for gravity wave and turbulent mountain stress parameterizations. The software supports regular latitude-longitude grids as well as unstructured grids; e.g. icosahedral, Voronoi, cubed-sphere and variable resolution grids.

As an example application and in the spirit of documenting model development, exploratory simulations illustrating the impacts of topographic smoothing with the NCAR-DOE CESM (Community Earth System Model) CAM5.2-SE (Community Atmosphere Model version 5.2 – Spectral Elements dynamical core) are shown.

1 Introduction

Accurate representation of the impact of topography on atmospheric flow is crucial for Earth system modeling. For example, the hydrological cycle is closely linked to topography and, on the planetary scale, waves associated with the mid-latitude jets are very susceptible to the effective drag caused by mountains (e.g., Lott and Miller, 1997). Despite the fact that surface elevation is known globally with a high level of precision, the representation of its impact on atmospheric flow in numerical models remains a challenge.

When performing a spectral analysis of high resolution elevation data (e.g., black line in Fig. 1), it is clear that Earth's topography decreases quite slowly with increasing wave number (see also Balmino, 1993; Uhrner, 2001; Gagnon et al., 2006). Consequently, at any practical model resolution there will always be a non-negligible spectral component of topography present near the grid scale and there will always be a non-negligible spectral component of topography below the grid-scale (sub-grid-scale

GMDD

8, 4623–4651, 2015

NCAR topography software

P. H. Lauritzen et al.

Title Page

Abstract

Introduction

Conclusions

References

Tables

Figures

◀

▶

◀

▶

Back

Close

Full Screen / Esc

Printer-friendly Version

Interactive Discussion



component). The resolved scale component is the mean elevation in each grid box h , or, equivalently¹, the surface geopotential Φ_s . It is common practice not to force the highest wave numbers directly in the model to alleviate obvious spurious noise (e.g. Navarra et al., 1994; Lander and Hoskins, 1997). Hence Φ_s is usually smoothed.

Figure 1 shows the power spectrum for surface elevation for different levels of smoothing of topography in the NCAR-DOE CESM (Community Earth System Model) CAM (Community Atmosphere Model; Neale et al., 2010) SE (Spectral Element; Thomas and Loft, 2005; Dennis et al., 2005) and CAM-FV (Finite-Volume; Lin, 2004). Figure 2 shows the associated elevations for a cross section through the Andes mountains. The amount of smoothing necessary is intrinsically linked to the numerical methods and discretization choices in the dynamical core. Further discussion on Φ_s smoothing is given in Sect. 3.2.

The component of topography that can not be represented by Φ_s is referred to as sub-grid-scale topography. Sub-grid-scale processes may be sub-grid flow blocking, flow splitting, sheltering effects, generation of turbulence by roughness and gravity wave breaking (e.g., Bougeault et al., 1990). These processes can have an important impact on the resolved scale flow. Global models usually have a parameterization for gravity wave drag (GWD) (e.g., Eckermann and Chun, 2003) and turbulent effects referred to as turbulent mountain stress (TMS). An increasing number of models also have a low-level blocking parameterization (e.g., Lott and Miller, 1997; Webster et al., 2003; Zadra et al., 2003; Kim and Doyle, 2005; Scinocca and McFarlane, 2000) and incorporate the effects of sub-grid-scale topographic anisotropy (i.e. the existence of ridges with dominant orientations used to determine the direction and magnitude of the drag exerted by sub-grid topography). The importance of anisotropy in quantifying topographic effects has been recognized for some time (e.g., Baines and Palmer, 1990; Bacmeister, 1993).

According to linear theory gravity waves can propagate in the vertical only when their intrinsic frequency is lower than the the Brunt–Väisälä frequency N (e.g., Dur-

¹if gravity is assumed constant

GMDD

8, 4623–4651, 2015

NCAR topography software

P. H. Lauritzen et al.

Title Page

Abstract

Introduction

Conclusions

References

Tables

Figures

◀

▶

◀

▶

Back

Close

Full Screen / Esc

Printer-friendly Version

Interactive Discussion



NCAR topography software

P. H. Lauritzen et al.

Title Page

Abstract

Introduction

Conclusions

References

Tables

Figures

◀

▶

◀

▶

Back

Close

Full Screen / Esc

Printer-friendly Version

Interactive Discussion



ran, 2003). For orographically-forced gravity waves the intrinsic frequency is set by the obstacle horizontal scale and the wind speed. When obstacle scales are too small to generate propagating waves we expect drag to be produced by unstratified turbulent flow, a process which is typically parameterized in models' TMS schemes. For larger obstacles we expect both drag and vertically-propagating waves to result, processes which are dealt by GWD schemes. Unfortunately the scale separating TMS and GWD processes is flow dependent. For typical midlatitude values of low-level wind (10 m s^{-1}) and N (10^{-2} s^{-1}) waves with wavelengths less than around 6000 m will not propagate in the vertical. A separation scale of 5000 m has been used by ECMWF (1997); Beljaars et al. (2004). Here we will generate two sub-grid-scale variables derived from the topography data: The variance of topography below the 6000 m scale (referred to as $\text{Var}^{(\text{TMS})}$) and the variance of topography with a scale longer than 6000 m and less than the grid scale (referred to as $\text{Var}^{(\text{GWD})}$).

It is the purpose of this paper to document a software package that, given a “raw” high resolution global elevation dataset, maps elevations data to any unstructured global grid and consistently separates the scales needed for TMS and GWD parameterizations. This separation of scales is done through an intermediate mapping of the raw elevation data to a 3000 m cubed-sphere grid ($\Lambda \rightarrow A$) before mapping fields to the target model grid ($A \rightarrow \Omega$) as schematically shown on Fig. 3. This two-step process is described in Sect. 2.2 after a mathematical definition of the scale-separation (Sect. 2.1). In Sect. 2.2.3 we briefly discuss Φ_s smoothing. In the spirit of model development some exploratory experiments illustrating the impacts of topographic smoothing with the NCAR-DOE CAM-SE and, for comparison CAM-FV, are presented in Sect. 3.2. Results from these experiments are shown to emphasize the importance of topographic smoothing rather than detailed investigation of the accuracy and process level analysis of how to most accurately model flow over topography.

2 Method

2.1 Continuous: separation of scales

The separation of scales is, in continuous space, conveniently introduced using spherical harmonics. Assume that elevation (above sea level) is a smooth continuous function in which case it can be represented by a convergent expansion of spherical harmonic functions of the form

$$h(\lambda, \theta) = \sum_{m=-\infty}^{\infty} \sum_{n=|m|}^{\infty} \psi_{m,n} Y_{m,n}(\lambda, \theta), \quad (1)$$

(e.g., Durran, 2010) where λ and θ are longitude and latitude, respectively, $\psi_{m,n}$ are the spherical harmonic coefficients. Each spherical harmonic function is given in terms of the associated Legendre polynomial $P_{m,n}(\theta)$:

$$Y_{m,n} = P_{m,n}(\theta) e^{im\lambda} \quad (2)$$

where m is the zonal wave number and $m - |n|$ is the number of zeros between the poles and can therefore be interpreted as meridional wave number.

For the separation of scales the spherical harmonic expansion is truncated at wave number M

$$h^{(M)}(\lambda, \theta) = \sum_{m=-M}^{\infty} \sum_{n=|m|}^M \psi_{m,n}^{(M)} Y_{m,n}(\lambda, \theta), \quad (3)$$

where a triangular truncation, which provides a uniform spatial resolution over the entire sphere, is used.

GMDD

8, 4623–4651, 2015

NCAR topography software

P. H. Lauritzen et al.

Title Page

Abstract

Introduction

Conclusions

References

Tables

Figures

◀

▶

◀

▶

Back

Close

Full Screen / Esc

Printer-friendly Version

Interactive Discussion



Let $h^{(\text{tgt})}(\lambda, \theta)$ be a continuous representation of the elevation containing the spatial scales of the target grid. We do not write $h^{(\text{tgt})}(\lambda, \theta)$ explicitly in terms of spherical harmonics as the target grid may be variable resolution and therefore contains different spatial scales in different parts of the domain.

For each target grid cell Ω_k , $k = 1, \dots, N_t$, where N_t is the number of target grid cells, define the variances

$$\text{Var}_{\Omega_k}^{(\text{tms})} = \iint_{\Omega_k} \left[h^{(M)}(\lambda, \theta) - h(\lambda, \theta) \right]^2 \cos(\theta) d\lambda d\theta, \quad (4)$$

$$\text{Var}_{\Omega_k}^{(\text{gwd})} = \iint_{\Omega_k} \left[h^{(\text{tgt})}(\lambda, \theta) - h^{(M)}(\lambda, \theta) \right]^2 \cos(\theta) d\lambda d\theta. \quad (5)$$

So $\text{Var}_{\Omega_k}^{(\text{tms})}$ is the variance of elevation on scales below wave number M and $\text{Var}_{\Omega_k}^{(\text{gwd})}$ is the variance of elevation on scales larger than wave number M and below the target grid scale.

2.2 Discrete: separation of scales

The separation of scales is done through the use of a quasi-isotropic gnomonic cubed-sphere grid in a two-step regridding procedure: binning from source grid Λ to intermediate grid A (separation of scales) and then rigorously remap variables to the target grid Ω .

Any quasi-uniform spherical grid could, in theory, be used for the separation of scales. For reasons that will become clear we have chosen to use a gnomonic cubed-sphere grid (see Fig. 3) resulting from an equi-angular gnomonic (central) projection

$$x = r \tan \alpha \quad \text{and} \quad y = r \tan \beta; \quad \alpha, \beta \in \left[-\frac{\pi}{4}, \frac{\pi}{4} \right], \quad (6)$$

(Ronchi et al., 1996) where α and β are central angles in each coordinate direction, $r = R/\sqrt{3}$ and R is the radius of the Earth. A point on the sphere is identified with the

Title Page

Abstract

Introduction

Conclusions

References

Tables

Figures

◀

▶

◀

▶

Back

Close

Full Screen / Esc

Printer-friendly Version

Interactive Discussion



[Title Page](#)[Abstract](#)[Introduction](#)[Conclusions](#)[References](#)[Tables](#)[Figures](#)[I ◀](#)[▶ I](#)[◀](#)[▶](#)[Back](#)[Close](#)[Full Screen / Esc](#)[Printer-friendly Version](#)[Interactive Discussion](#)

three-element vector (x, y, ν) , where ν is the panel index. Hence the physical domain S (sphere) is represented by the gnomonic (central) projection of the cubed-sphere faces, $\Omega^{(\nu)} = [-1, 1]^2$, $\nu = 1, 2, \dots, 6$, and the non-overlapping panel domains $\Omega^{(\nu)}$ span the entire sphere: $S = \bigcup_{\nu=1}^6 \Omega^{(\nu)}$. The cube edges, however, are discontinuous. Note that any straight line on the gnomonic projection (x, y, ν) corresponds to a great-circle arc on the sphere. In the discretized scheme we let the number of cells along a coordinate axis be N_c so that the total number of cells in the global domain is $6 \times N_c^2$. The grid lines are separated by the same angle $\Delta\alpha = \Delta\beta = \frac{\pi}{2N_c}$ in each coordinate direction.

For notational simplicity the cubed-sphere cells are identified with one index i and the relationship between i and $(\text{icube}, \text{jcube}, \nu)$ is given by

$$i = \text{icube} + (\text{jcube} - 1)N_c + (\nu - 1)N_c^2, \quad (7)$$

where $(\text{icube}, \text{jcube}) \in [1, \dots, N_c]^2$ and $\nu \in [1, 2, \dots, 6]$. In terms of central angles (α, β) the cubed-sphere grid cell i is defined as

$$A_i = \left[\left((\text{icube} - 1)\Delta\alpha - \frac{\pi}{4}, \text{icube}\Delta\alpha - \frac{\pi}{4} \right) \right. \\ \left. \times \left[(\text{jcube} - 1)\Delta\beta - \frac{\pi}{4}, \text{jcube}\Delta\beta - \frac{\pi}{4} \right], \right] \quad (8)$$

and ΔA_i denotes the associated spherical area. A formula for the spherical area ΔA_i of a grid cell on the gnomonic cubed-sphere grid can be found in Appendix C of Lauritzen and Nair (2008) (note that Eq. C3 is missing arccos on the right-hand side). A quasi-uniform approximately 3000 m resolution is obtained by using $N_c = 3000$ which results in a scale separation of roughly 6000 m. For more details on the construction of the gnomonic grid see, e.g., Lauritzen et al. (2010).

2.2.1 Step 1: raw elevation data to intermediate cubed-sphere grid ($\Lambda \rightarrow A$)

The “raw” elevation data is usually from a digital elevation model (DEM) such as the GTOPO30; a 30 arc second global dataset from the United States Geological Survey

(USGS; Gesch and Larson, 1998) defined on an approximately 1 km regular latitude-longitude grid. Several newer, more accurate, and locally higher resolution elevation datasets are available such as GLOBE (GLOBE Task Team and others, 1999) and the NASA Shuttle Radar Topographic Mission (SRTM) DEM data (Farr et al., 2007). The SRTM data, however, is only near-global (up to 60° North and South). Here we use GTOPO30. The data comes in 33 tiles (separate files) in 16-bit binary format. Fortran code is provided to convert the data into one NetCDF file. Even though the elevation is stored as integers the size of the NetCDF file is 7 GB. The GTOPO file contains height h and landfraction $LANDFRAC$ (for the mathematical operations below we use f to refer to land fraction).

The center of the regular latitude-longitude grid cells for the “raw” topographic data are denoted $(\lambda_{ilon}, \theta_{jlat})$, $ilon = 1, \dots, nlon$, $jlat = 1, \dots, nlat$. For the USGS dataset used here $nlon = 43200$ and $nlat = 21600$. As for the cubed-sphere we use one index j to reference the grid cells

$$j = ilon + (jlat - 1) \times nlon, \quad j \in [1, \dots, N_r], \quad (9)$$

where $N_r = nlon \times nlat$. The spherical area of grid cell Λ_j is denoted $\Delta\Lambda_j$ and the average elevation in cell j is given by $h_{\Lambda_j}^{(raw)}$.

This data is binned to the cubed-sphere intermediate grid by identifying in which gnomonic cubed-sphere grid cell $(\lambda_{ilon}, \theta_{jlat})$ is located. Due to the “Cartesian”-like structure of the cubed-sphere grid the search algorithm is straight forward (following Nair et al., 2005):

- transform $(\lambda_{ilon}, \theta_{jlat})$ coordinate to Cartesian coordinates (x, y, z) :

$$x = \cos(\lambda_{ilon}) \cos(\theta_{jlat}),$$

$$y = \sin(\lambda_{ilon}) \cos(\theta_{jlat}),$$

$$z = \sin(\theta_{jlat}).$$

GMDD

8, 4623–4651, 2015

NCAR topography software

P. H. Lauritzen et al.

Title Page

Abstract

Introduction

Conclusions

References

Tables

Figures

⏪

⏩

◀

▶

Back

Close

Full Screen / Esc

Printer-friendly Version

Interactive Discussion



- locate which cubed-sphere panel $(\lambda_{i\text{lon}}, \theta_{i\text{lat}})$ is located on through a “coordinate maximality” algorithm, i.e. let

$$\text{pm} = \max(|x|, |y|, |z|),$$

then if

- $\text{pm} = |x|$ and $x > 0$ then $(\lambda_{i\text{lon}}, \theta_{i\text{lat}})$ is on $\nu = 1$.
 - $\text{pm} = |y|$ and $y > 0$ then $(\lambda_{i\text{lon}}, \theta_{i\text{lat}})$ is on $\nu = 2$.
 - $\text{pm} = |x|$ and $x < 0$ then $(\lambda_{i\text{lon}}, \theta_{i\text{lat}})$ is on $\nu = 3$.
 - $\text{pm} = |y|$ and $y < 0$ then $(\lambda_{i\text{lon}}, \theta_{i\text{lat}})$ is on $\nu = 4$.
 - $\text{pm} = |z|$ and $z \leq 0$ then $(\lambda_{i\text{lon}}, \theta_{i\text{lat}})$ is located on the bottom panel, $\nu = 5$.
 - $\text{pm} = |z|$ and $z > 0$ then $(\lambda_{i\text{lon}}, \theta_{i\text{lat}})$ is located on the top panel, $\nu = 6$.
- Given the panel number the associated central angles (α, β) are given by:
- $\nu = 1: (\alpha, \beta) = \left[\arctan\left(\frac{x}{z}\right), \arctan\left(\frac{y}{z}\right) \right]$.
 - $\nu = 2: (\alpha, \beta) = \left[\arctan\left(\frac{-x}{y}\right), \arctan\left(\frac{z}{y}\right) \right]$.
 - $\nu = 3: (\alpha, \beta) = \left[\arctan\left(\frac{-y}{-x}\right), \arctan\left(\frac{y}{-x}\right) \right]$.
 - $\nu = 4: (\alpha, \beta) = \left[\arctan\left(\frac{x}{-y}\right), \arctan\left(\frac{z}{-y}\right) \right]$.
 - $\nu = 5: (\alpha, \beta) = \left[\arctan\left(\frac{y}{-z}\right), \arctan\left(\frac{x}{-z}\right) \right]$.
 - $\nu = 6: (\alpha, \beta) = \left[\arctan\left(\frac{y}{z}\right), \arctan\left(\frac{-x}{z}\right) \right]$.

Title Page

Abstract

Introduction

Conclusions

References

Tables

Figures

◀

▶

◀

▶

Back

Close

Full Screen / Esc

Printer-friendly Version

Interactive Discussion



- the indices of the cubed-sphere cell in which the center of the latitude-longitude grid cell is located is given by

$$\text{icube} = \text{CEILING} \left(\frac{\alpha + \frac{\pi}{4}}{\Delta\alpha} \right),$$

$$\text{jcube} = \text{CEILING} \left(\frac{\beta + \frac{\pi}{4}}{\Delta\beta} \right),$$

where the `CEILING(.)` function returns the smallest integer not less than the argument.

The set of indices for which center points of regular latitude-longitude grid cells are located in gnomonic cubed-sphere cell A_i is denoted \mathcal{S}_i . Note that since the USGS dataset is higher resolution than the cubed-sphere \mathcal{S}_i is guaranteed to be non-empty.

Through this binning process the approximate average elevation in cubed-sphere cell i becomes

$$\bar{h}_{A_i}^{(\text{cube})} = \frac{1}{\Delta A_i} \sum_{j \in \mathcal{S}_i} h_{\Gamma_j}^{(\text{raw})} \Delta \Lambda_j. \quad (10)$$

When $\bar{h}_{A_i}^{(\text{cube})}$ is known we can compute the sub-grid variance on the intermediate cubed-sphere grid A :

$$\text{Var}_{A_i}^{(\text{tms})} = \frac{1}{\Delta A_i} \sum_{j \in \mathcal{S}_i} \left(\bar{h}_{A_i}^{(\text{cube})} - h_{\Gamma_j}^{(\text{raw})} \right)^2 \Delta \Lambda_j. \quad (11)$$

The land fraction is also binned to the intermediate cubed-sphere grid

$$\bar{f}_{A_i}^{(\text{cube})} = \frac{1}{\Delta A_i} \sum_{j \in \mathcal{S}_i} f_{\Gamma_j}^{(\text{raw})} \Delta \Lambda_j. \quad (12)$$

Title Page

Abstract

Introduction

Conclusions

References

Tables

Figures

◀

▶

◀

▶

Back

Close

Full Screen / Esc

Printer-friendly Version

Interactive Discussion



To remain consistent with previous topography generation software for CAM all land-fractions South of 79° S are set to one which effectively extends the land for the Ross Ice shelf.

The binning process is straight forward since the cubed-sphere grid is essentially an equidistant Cartesian grid on each panel in terms of the central angle coordinates. This step could be replaced by rigorous remapping in terms of overlap areas between the regular latitude-longitude grid and the cubed-sphere grid using the geometrically exact algorithm of (Ullrich et al., 2009) optimized for the regular latitude-longitude and gnomonic cubed-sphere grid pair or the more general remapping algorithm called SCRIP (Jones, 1999).

2.2.2 Step 2: cubed-sphere grid to target grid ($A \rightarrow \Omega$)

The cell averaged values of elevation and sub-grid-scale variances ($\text{Var}_{\Omega}^{(\text{tms})}$ and $\text{Var}_{\Omega}^{(\text{gwd})}$) on the target grid are computed by rigorously remapping the variables from the cubed-sphere grid to the target grid. The remapping is performed using CSLAM (Conservative Semi-Lagrangian Multi-tracer transport scheme) technology (Lauritzen et al., 2010) that has the option for performing higher-order remapping. It is possible to use large parts of the CSLAM technology since the source grid is a gnomonic cubed-sphere grid hence instead of remapping between the gnomonic cubed-sphere grid and a deformed Lagrangian grid, as done in CSLAM transport, the remapping is from the gnomonic cubed-sphere grid to any target grid constructed from great-circle arcs (the target grid “plays the role” of the Lagrangian grid). However, a couple of modifications were made to the CSLAM search algorithm. First of all, the target grid cells can have an arbitrary number of vertices whereas the CSLAM transport search algorithm assumes that the target grid consists of quadrilaterals and the number of overlap areas are determined by the deformation of the transporting velocity field. In the case of the remapping needed in this application the target grid consists of polygons with any number of vertices and the search is not constrained by the physical relation between

Title Page

Abstract

Introduction

Conclusions

References

Tables

Figures

◀

▶

◀

▶

Back

Close

Full Screen / Esc

Printer-friendly Version

Interactive Discussion



regular and deformed upstream quadrilaterals. Secondly, the CSLAM search algorithm for transport assumes that the target grid cells are convex which is not necessarily the case for target grids. The CSLAM search algorithm has been modified to support non-convex cells that are, for example, encountered in variable resolution CAM-SE (see Fig. 4); essentially that means that any target grid cell may cross a gnomonic isoline (source grid line) more than twice.

Let the target grid consist of N_t grid cells Ω_k , $k = 1, \dots, N_t$ with associated spherical area $\Delta\Omega_k$. The search algorithm for CSLAM is used to identify overlap areas between the target grid cell Ω_k and the cubed-sphere grid cells A_ℓ , $\ell = 1, \dots, N_c$. Denote the overlap area between Ω_k and A_ℓ

$$\Omega_{k\ell} = \Omega_k \cap A_\ell, \quad (13)$$

(see Fig. 5) and let L_k denote the set of indices for which $\Omega_k \cap A_\ell$, $\ell = 1, \dots, N_c$, is non-empty. Then the average elevation and variance used for TMS in target grid cell k are given by

$$\overline{h}_{\Omega_k}^{-(\text{tgt,raw})} = \frac{1}{\Delta\Omega_k} \sum_{\ell \in L_k} \overline{h}_{A_\ell}^{-(\text{cube})} \Delta\Omega_{k\ell}, \quad (14)$$

$$\overline{\text{Var}}_{\Omega_k}^{-(\text{tms})} = \frac{1}{\Delta\Omega_k} \sum_{\ell \in L_k} \overline{\text{Var}}_{\Omega_\ell}^{-(\text{tms})} \Delta\Omega_{k\ell}, \quad (15)$$

respectively. The variance of the cubed-sphere data $\overline{h}^{-(\text{cube})}$ with respect to the target grid cell average values $\overline{h}^{-(\text{tgt,raw})}$ is given by

$$\overline{\text{Var}}_{\Omega_k}^{-(\text{gwd,raw})} = \frac{1}{\Delta\Omega_k} \sum_{\ell \in L_k} \left(\overline{h}_{\Omega_k}^{-(\text{tgt,raw})} - \overline{h}_{A_\ell}^{-(\text{cube})} \right)^2 \Delta\Omega_{k\ell}, \quad (16)$$

The appended superscript raw in $\overline{h}^{-(\text{tgt,raw})}$ and $\overline{\text{Var}}^{-(\text{gwd,raw})}$ refers to the fact that the elevation and GWD variance is based on unsmoothed elevation. As mentioned in the

Title Page

Abstract

Introduction

Conclusions

References

Tables

Figures

◀

▶

◀

▶

Back

Close

Full Screen / Esc

Printer-friendly Version

Interactive Discussion



introduction the elevation is usually smoothed i.e. the highest wave number are removed. This smoothed elevation is denoted

$$\overline{h}^{-(tgt,smooth)} \quad (17)$$

Note that after smoothing the target grid elevation the sub-grid scale variance for GWD should be recomputed as the smoothing operation will add energy to the smallest wave lengths:

$$\overline{\text{Var}}_{\Omega_k}^{-(gwd,smooth)} = \frac{1}{\Delta\Omega_k} \sum_{\ell \in \mathbb{L}_k} \left(\overline{h}_{\Omega_k}^{-(tgt,smooth)} - \overline{h}_{A_\ell}^{-(cube)} \right)^2 \Delta\Omega_{k\ell}. \quad (18)$$

The smoothing of elevation is discussed in some detail in the next section.

2.2.3 Smoothing of elevation $\overline{h}_\Omega^{(tgt)}$

As discussed in the introduction the raw topographic data mapped to the target grid without further filtering to remove the highest wave numbers usually leads to excessive spurious noise in the simulations. There seem to be no standardized procedure, for example a test case suite, to objectively select the level of smoothing and filtering method. The amount of smoothing necessary to remove spurious noise in, e.g. vertical velocity, depends on the amount of inherent or explicit numerical diffusion in the dynamical core (e.g., Lauritzen et al., 2011). It may be considered important that the topographic smoothing is done with discrete operators consistent with the dynamical core.

While it is necessary to smooth topography to remove spurious grid-scale noise, it potentially introduces two problems. Filtering will typically raise ocean points near step topography to non-zero elevation. Perhaps the most striking example is the Andes mountain range that extends one or two grid cells into the Pacific after the filtering operation (Fig. 2). Ocean and land points are treated separately in weather/climate

Title Page

Abstract

Introduction

Conclusions

References

Tables

Figures

⏪

⏩

◀

▶

Back

Close

Full Screen / Esc

Printer-friendly Version

Interactive Discussion



GMDD

8, 4623–4651, 2015

NCAR topography software

P. H. Lauritzen et al.

Title Page

Abstract

Introduction

Conclusions

References

Tables

Figures

I◀

▶I

◀

▶

Back

Close

Full Screen / Esc

Printer-friendly Version

Interactive Discussion



models so raised sea-points may potentially be problematic. Secondly, the filtering will generally reduce the height of local topographic maxima and given the importance of barrier heights in atmospheric dynamics, this could be a problem for the global angular momentum budget and could fundamentally change the flow (unless a parameterization for blocking is used). To capture more of the barrier effect (blocking), two approaches have been put forward in the literature to deepen valleys and increase peak heights while filtering out small scales: *envelope topography* adjusts the surface height with sub-grid scale topographic variance (Wallace et al., 1983; Mesinger and Strickler, 1982). Loosely speaking, the otherwise smoothed peak heights are raised. This process may perturb the average surface height. Alternatively, one may use Silhouette averaging (Smart et al., 2005; Walko and Tremback, 2004; Bossert, 1990). A similar approach, but implemented as variational filtering, is taken in Rutt et al. (2006); this method also imposes additional constraints such as enforcing zero elevation over ocean masks.

As there is no standard procedure for smoothing topography, we leave it up to the user to smooth the raw topography $\bar{h}^{-(tgt,raw)}$. The smoothed topography is referred to as $\bar{h}^{-(tgt,smooth)}$. As mentioned before $\overline{\text{Var}}_{\Omega_k}^{(gwd,smooth)}$ must be recomputed after smoothing \bar{h} as the filtering operation will transfer energy to the sub-grid-scale.

2.3 Naming conventions

The naming conventions for the topographic variables in the software and NetCDF files is:

$$PHIS = g h_{\Omega}^{-(tgt)}, \quad (19)$$

$$SGH = \sqrt{\text{Var}_{\Omega}^{(gwd)}}, \quad (20)$$

$$SGH30 = \sqrt{\text{Var}_{\Omega}^{(tms)}}, \quad (21)$$

$$LANDFRAC = \bar{f}_{\Omega}^{-(tgt)}, \quad (22)$$

where g is the gravitational constant.

3 Results

Exploratory simulations illustrating the effects of topographic smoothing on some climate diagnostics in CAM are shown.

3.1 Smoothing methods used in CAM-FV and CAM-SE

In the CAM-FV the highest wave-numbers are removed by mapping Φ_s (surface geopotential) to a regular latitude-longitude grid that is half the resolution of the desired model resolution, and then map back to the model grid by one-dimensional remaps along latitudes and longitudes, respectively, using the PPM (Piecewise Parabolic Method) with monotone filtering. In CAM-SE the surface geopotential is smoothed by multiple applications of the CAM-SE Laplace operator combined with a bounds preserving limiter. Figure 2 shows different levels of smoothing of surface height for CAM-SE and for comparison CAM-FV. It can clearly be seen that there are large differences between the height of the mountains with different smoothing operators and smoothing strength.

3.2 Example topography smoothing experiments with CAM-SE

CAM-SE uses the spectral element dynamical core from HOMME (High-Order Method Modeling Environment; Thomas and Loft, 2005; Dennis et al., 2005). CESM tag `cesm1_1_0_re106` with the FAMIPC5 compset is used². The model is run at approximately 1° resolution which is the NE30NP4 configuration with 30 × 30 elements on each cubed-sphere panel and 4 × 4 Gauss-Lobatto-Legendre (GLL) quadrature points in each element. The default hyperviscosity coefficient is $\nu = 1 \times 10^{15} \text{ m}^4 \text{ s}^{-1}$.

Results are shown for 30 year AMIP-style runs (CESM FAMIPC5 compset). Simulations were performed with different levels of smoothing of topography and changes to the divergence damping parameter. The level of smoothing follows the naming convention defined in the caption of Fig. 1. The $1 \times \text{div}$ refers to the same level of damping of vortical and divergent modes (fourth-order hyperviscosity with damping coefficient $\nu = 1 \times 10^{15} \text{ m}^4 \text{ s}^{-1}$). Experiments are run for which the divergent modes are damped with a coefficient that is 2.5² and 5² times larger than the damping coefficient for the vortical modes.

Figure 7 shows results from AMIP simulations with CAM-SE using different levels of Φ_s smoothing and numerical diffusion of divergent modes. Spurious noise near steep topography is apparent in vertical velocity ω (top panels) for model configurations with weak smoothing and divergence damping. Effects on important hydrological fields such as precipitation are also evident although they are somewhat less pronounced. As already noted, there are not commonly accepted measures of what constitutes a reasonable level of apparently spurious small-scale variability in climate simulation variables. Smoothing of topography can itself have negative effects. We note for example in the precipitation plots shown in Fig. 7 that smoothing Φ_s does nothing to remove the large moist bias present over the Himalayan front, in fact smoothing is arguably increasing the extent of the bias. The detailed dynamics behind these improvements is not yet understood, but there connection to rougher topography is clear.

²CAM version 5.2 in which SE uses Eulerian vertical advection

Figure 8 shows the total kinetic energy spectra (TKE) for the different model configurations. The energy associated with vortical modes is not significantly by the roughness of the topography or the strength of the divergence damping. Obviously the energy associated with divergent modes is directly related to the divergence damping coefficient but the roughness of the topography does not appear to have any significant effect on the tail of the TKE energy spectrum for divergence (these results, however, may change at higher horizontal resolutions).

4 Conclusions

The NCAR global model topography generation software for unstructured grids has been documented and example applications to CAM have been presented. The topography software consistently computes sub-grid scale variances using a quasi-isotropic separation of scales through the intermediate mapping of high resolution elevation data to an equi-angular cubed-sphere grid. The software supports structured or unstructured (e.g., variable resolution) global grid.

Code availability

The source codes for the NCAR Global Model Topography Generation Software for Unstructured Grid are available at through Github. The repository URL is <https://github.com/UCAR/Topo/tags/>. The repository also contains NCL scripts to plot the topography variables (Fig. 6) that the software generates.

Acknowledgements. NCAR is sponsored by the National Science Foundation (NSF). Mark Taylor was supported by the Department of Energy Office of Biological and Environmental Research, work package 12-015334 “Multiscale Methods for Accurate, Efficient, and Scale-Aware Models of the Earth System”. Thanks to Sang-hun Park (NCAR) for providing data for the GTOPO30 power spectrum.



References

- Bacmeister, J.: Mountain-wave drag in the stratosphere and mesosphere inferred from observed winds and a simple mountain-wave parameterization scheme, *J. Atmos. Sci.*, 50, 377–399, doi:10.1175/1520-0469, 1993. 4625
- 5 Baines, P. and Palmer, T.: Rationale for a new physically based parametrization of subgrid-scale orographic effects, ECMWF Tech. Memo., 1699, 1990. 4625
- Balmino, G.: The Spectra of the topography of the Earth, Venus and Mars, *Geophys. Res. Lett.*, 20, 1063–1066, doi:10.1029/93GL01214, 1993. 4624
- Beljaars, A., Brown, A., and Wood, N.: A new parametrization of turbulent orographic form drag, *Q. J. Roy. Meteor. Soc.*, 130, 1327–1347, doi:10.1256/qj.03.73, 2004. 4626
- 10 Bossert, J. E.: Regional-scale flow in complex terrain: An observational and numerical investigation, PhD thesis, Colorado State Univ., Fort Collins, USA, 1990. 4636
- Bougeault, P., Clar, A. J., Benech, B., Carissimo, B., Pelon, J., and Richard, E.: Momentum Budget over the Pyrénées: The PYREX Experiment, *B. Am. Meteorol. Soc.*, 71, 806–818, 1990. 4625
- 15 Dennis, Fournier, A., Spitz, W. F., St-Cyr, A., Taylor, M. A., Thomas, S. J., and Tufo, H.: High-Resolution Mesh Convergence Properties and Parallel Efficiency of a Spectral Element Atmospheric Dynamical Core, *Int. J. High Perform. Comput. Appl.*, 19, 225–235, doi:10.1177/1094342005056108, 2005. 4625, 4638
- 20 Durran, D.: Lee waves and mountain waves, in: *Encyclopedia of Atmospheric Sciences*, edited by: Holton, J. R., 1161–1169, Academic Press, London, UK, doi:10.1016/B0-12-227090-8/00202-5, 2003. 4625
- Durran, D.: *Numerical Methods for Fluid Dynamics: With Applications to Geophysics*, vol. 32 of *Texts in Applied Mathematics*, 2 edn., Springer, New York, USA, 516 pp., 2010. 4627
- 25 Eckermann, Y. K. S. and Chun, H.-Y.: An overview of the past, present and future of gravity-wave drag parametrization for numerical climate and weather prediction models: survey article, *Atmos. Ocean*, 41, 65–98, doi:10.3137/ao.410105, 2003. 4625
- ECMWF: *Proceedings of a workshop on orography*, ECMWF, Reading, UK, 1997. 4626
- Farr, T. G., Rosen, P. A., Caro, E., Crippen, R., Duren, R., Hensley, S., Kobrick, M., Paller, M., Rodriguez, E., Roth, L., Seal, D., Shaffer, S., Shimada, J., Umland, J., Werner, M., Oskin, M., Burbank, D., and Alsdorf, D.: The Shuttle Radar Topography Mission, *Rev. Geophys.*, 45, 1–33, doi:10.1029/2005RG000183, 2007. 4630

Title Page

Abstract

Introduction

Conclusions

References

Tables

Figures

⏪

⏩

◀

▶

Back

Close

Full Screen / Esc

Printer-friendly Version

Interactive Discussion



[Title Page](#)[Abstract](#)[Introduction](#)[Conclusions](#)[References](#)[Tables](#)[Figures](#)[I◀](#)[▶I](#)[◀](#)[▶](#)[Back](#)[Close](#)[Full Screen / Esc](#)[Printer-friendly Version](#)[Interactive Discussion](#)

- Gagnon, J.-S., Lovejoy, S., and Schertzer, D.: Multifractal earth topography, *Nonlinear Proc. Geoph.*, 13, 541–570, doi:10.5194/npg-13-541-2006, 2006. 4624
- Gesch, D. B. and Larson, K. S.: Techniques for development of global 1-kilometer digital elevation models, in: *Pecora Thirteenth Symposium, Am. Soc. Photogrammetry Remote Sens.*, 5 Soix Falls, South Dakota, 1998. 4630
- GLOBE Task Team and others: The Global Land One-kilometer Base Elevation (GLOBE) Digital Elevation Model, Version 1.0, available at: <http://www.ngdc.noaa.gov/mgg/topo/globe.html> (last access: 18 June 2015), 1999. 4630
- Jones, P. W.: First- and Second-Order Conservative Remapping Schemes for Grids in Spherical 10 Coordinates, *Mon. Weather Rev.*, 127, 2204–2210, 1999. 4633
- Kim, Y.-J. and Doyle, J. D.: Extension of an orographic-drag parametrization scheme to incorporate orographic anisotropy and flow blocking, *Q. J. Roy. Meteor. Soc.*, 131, 1893–1921, doi:10.1256/qj.04.160, 2005. 4625
- Lander, J. and Hoskins, B.: Believable scales and parameterizations in a spectral transform 15 model, *Mon. Weather Rev.*, 125, 292–303, doi:10.1175/1520-0493, 1997. 4625
- Lauritzen, P. H. and Nair, R. D.: Monotone and conservative Cascade Remapping between Spherical grids (CaRS): Regular latitude-longitude and cubed-sphere grids., *Mon. Weather Rev.*, 136, 1416–1432, 2008. 4629
- Lauritzen, P. H., Nair, R. D., and Ullrich, P. A.: A conservative semi-Lagrangian multi-tracer 20 transport scheme (CSLAM) on the cubed-sphere grid, *J. Comput. Phys.*, 229, 1401–1424, doi:10.1016/j.jcp.2009.10.036, 2010. 4629, 4633
- Lauritzen, P. H., Mirin, A., Truesdale, J., Raeder, K., Anderson, J., Bacmeister, J., and Neale, R. B.: Implementation of new diffusion/filtering operators in the CAM-FV dynamical core, *Int. J. High Perform. Comput. Appl.*, 26, 63–73, doi:10.1177/1094342011410088, 2011. 4635
- Lin, S.-J.: A 'Vertically Lagrangian' Finite-Volume Dynamical Core for Global Models, *Mon. 25 Weather Rev.*, 132, 2293–2307, 2004. 4625
- Lott, F. and Miller, M. J.: A new subgrid-scale orographic drag parametrization: Its formulation and testing, *Q. J. Roy. Meteor. Soc.*, 123, 101–127, doi:10.1002/qj.49712353704, 1997. 4624, 4625
- Mesinger, F. and Strickler, R. F.: Effect of Mountains on Genoa Cyclogenesis, *J. Meteorol. Soc. 30 Jpn.*, 60, 326–337, 1982. 4636
- Nair, R. D., Thomas, S. J., and Loft, R. D.: A Discontinuous Galerkin Transport Scheme on the Cubed Sphere, *Mon. Weather Rev.*, 133, 814–828, 2005. 4630

Title Page

Abstract

Introduction

Conclusions

References

Tables

Figures

I◀

▶I

◀

▶

Back

Close

Full Screen / Esc

Printer-friendly Version

Interactive Discussion



- Navarra, A., Stern, W. F., and Miyakoda, K.: Reduction of the Gibbs Oscillation in Spectral Model Simulations, *J. Climate*, 7, 1169–1183, 1994. 4625
- Neale, R. B., Chen, C.-C., Gettelman, A., Lauritzen, P. H., Park, S., Williamson, D. L., Conley, A. J., Garcia, R., Kinnison, D., Lamarque, J.-F., Marsh, D., Mills, M., Smith, A. K., Tilmes, S., Vitt, F., Cameron-Smith, P., Collins, W. D., Iacono, M. J., Easter, R. C., Ghan, S. J., Liu, X., Rasch, P. J., and Taylor, M. A.: Description of the NCAR Community Atmosphere Model (CAM 5.0), NCAR Technical Note, National Center of Atmospheric Research, Boulder, Colorado, USA, 2010. 4625
- Ronchi, C., Iacono, R., and Paolucci, P. S.: The “Cubed Sphere”: A New Method for the Solution of Partial Differential Equations in Spherical Geometry, *J. Comput. Phys.*, 124, 93–114, 1996. 4628
- Rutt, I., Thuburn, J., and Staniforth, A.: A variational method for orographic filtering in NWP and climate models, *Q. J. Roy. Meteor. Soc.*, 132, 1795–1813, doi:10.1256/qj.05.133, 2006. 4636
- Scinocca, J. and McFarlane, N.: The parametrization of drag induced by stratified flow over anisotropic orography, *Q. J. Roy. Meteor. Soc.*, 126, 2353–2393, doi:10.1002/qj.49712656802, 2000. 4625
- Skamarock, W. C., Klemp, J. B., Duda, M. G., Fowler, L., Park, S.-H., and Ringler, T. D.: A Multi-scale Nonhydro- static Atmospheric Model Using Centroidal Voronoi Tessellations and C-Grid Staggering, *Mon. Weather Rev.*, 240, 3090–3105, doi:10.1175/MWR-D-11-00215.1, 2012. 4646
- Smart, J., Shaw, B., and McCaslin, P.: WRF SI V2.0: Nesting and details of terrain processing, 13, available at: <http://www.wrf-model.org/si/WRFSI-V2.0-Nesting-Ter-Proc.pdf> (last access: 18 June 2015), 2005. 4636
- Thomas, S. J. and Loft, R. D.: The NCAR Spectral Element Climate Dynamical Core: Semi-Implicit Eulerian Formulation, *J. Sci. Comput.*, 25, 307–322, 2005. 4625, 4638
- Uhrner, U.: The impact of new sub-grid scale orography fields on the ECMWF model, ECMWF Tech. Memo., 329, 2001. 4624
- Ullrich, P. A., Lauritzen, P. H., and Jablonowski, C.: Geometrically Exact Conservative Remapping (GECORE): Regular latitude-longitude and cubed-sphere grids, *Mon. Weather Rev.*, 137, 1721–1741, 2009. 4633
- Walko, R. and Tremback, C. J.: RAMS, Regional Atmospheric Modeling System, Version 4.3/4.4, Model Input Namelist Parameters, Boulder, Colorado, USA, 2004. 4636

- Wallace, J. M., Tibaldi, S., and Simmons, A. J.: Reduction of systematic forecast errors in the ECMWF model through the introduction of an envelope orography, *Q. J. Roy. Meteor. Soc.*, 109, 683–717, doi:10.1002/qj.49710946202, 1983. 4636
- 5 Webster, S., Brown, A. R., Cameron, D. R., and P.Jones, C.: Improvements to the representation of orography in the Met Office Unified Model, *Q. J. Roy. Meteor. Soc.*, 129, 1989–2010, 2003. 4625
- Zadra, A., Roch, M., Laroche, S., and Charron, M.: The subgrid-scale orographic blocking parametrization of the GEM Model, *Atmos. Ocean*, 41, 155–170, doi:10.3137/ao.410204, 2003. 4625

GMDD

8, 4623–4651, 2015

NCAR topography software

P. H. Lauritzen et al.

Title Page

Abstract

Introduction

Conclusions

References

Tables

Figures



Back

Close

Full Screen / Esc

Printer-friendly Version

Interactive Discussion



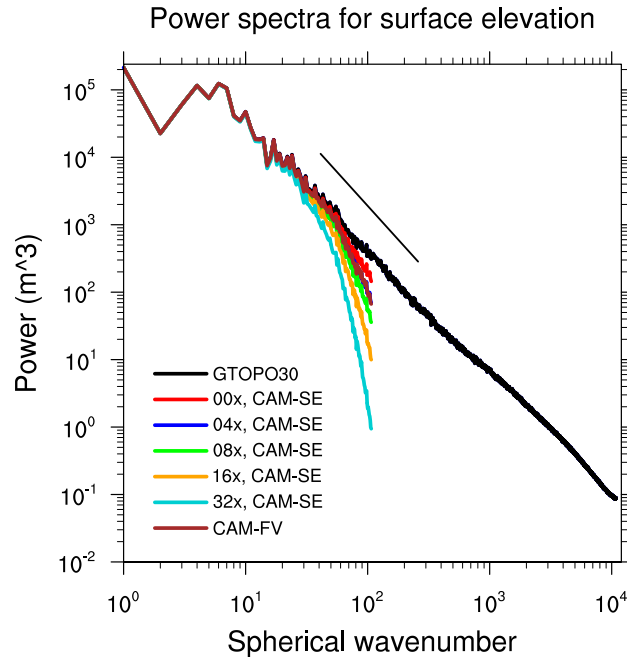


Figure 1. Log/log plot of spectral energy versus wave number K for the “raw” 1 km USGS data (GTOPO30), different levels of smoothing for 100 km CAM-SE topography, and CAM-FV. Labels 04x, 08x, 16x and 32x CAM-SE, refer to different levels of smoothing, more precisely, four, eight, sixteen and thirty two applications of a “Laplacian” smoothing operator in CAM-SE, respectively. Label CAM-FV refers to the topography used in CAM-FV at $0.9^\circ \times 1.25^\circ$ resolution. 0x CAM-SE is the unsmoothed topography on an approximately 1° grid CAM-SE grid. Note that the blue (4x, CAM-SE) and brown (CAM-FV) lines are overlaying. Solid straight line shows the K^{-2} slope. The associated surface elevations are shown on Fig. 2.

Title Page	
Abstract	Introduction
Conclusions	References
Tables	Figures
◀	▶
◀	▶
Back	Close
Full Screen / Esc	
Printer-friendly Version	
Interactive Discussion	



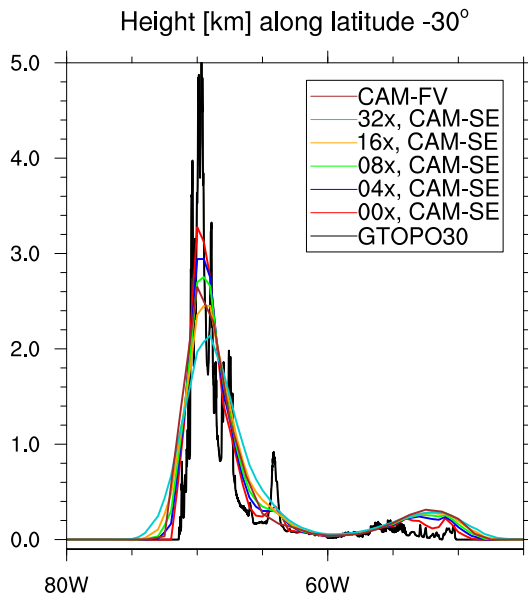


Figure 2. Surface elevation in kilometers for a cross section along latitude 30° S (through Andes mountain range) for different representations of surface elevation. The labeling is the same as in Fig. 1.

Title Page

Abstract Introduction

Conclusions References

Tables Figures

◀ ▶

◀ ▶

Back Close

Full Screen / Esc

Printer-friendly Version

Interactive Discussion



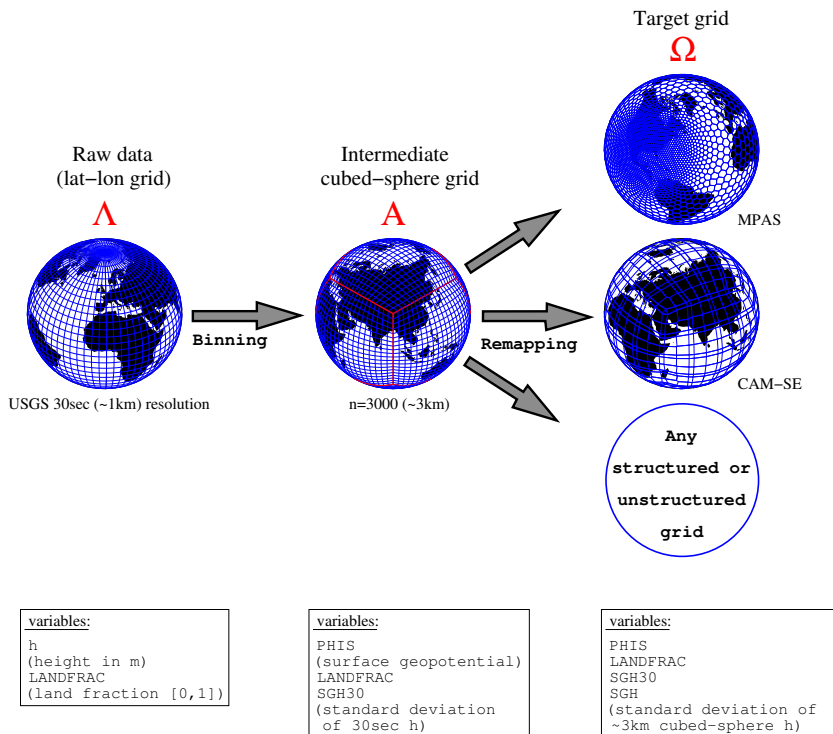


Figure 3. A schematic showing the regridding procedure. Red fonts refer to the naming conventions for the grids: Λ is the “raw” data grid (1 km regular lat-lon grid), A is the intermediate cubed-sphere grid and Ω is the target grid which may be any unstructured or structured grid. The variable naming conventions in the boxes are explained in Sect. 2.3. Data for the variable resolution MPAS (Model for Prediction Across Scales; Skamarock et al., 2012) grid plot is courtesy of W. C. Skamarock (NCAR).

Title Page

Abstract	Introduction
Conclusions	References
Tables	Figures

⏪
⏩
⏴
⏵

Back
Close

Full Screen / Esc

Printer-friendly Version

Interactive Discussion



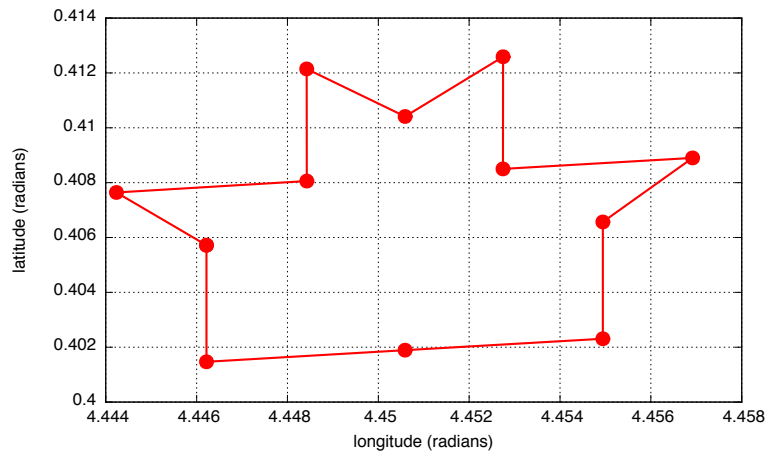


Figure 4. An example of a non-convex control volume in variable resolution CAM-SE. Vertices are filled circles and they are connected with straight lines.

[Title Page](#)[Abstract](#)[Introduction](#)[Conclusions](#)[References](#)[Tables](#)[Figures](#)[I◀](#)[▶I](#)[◀](#)[▶](#)[Back](#)[Close](#)[Full Screen / Esc](#)[Printer-friendly Version](#)[Interactive Discussion](#)

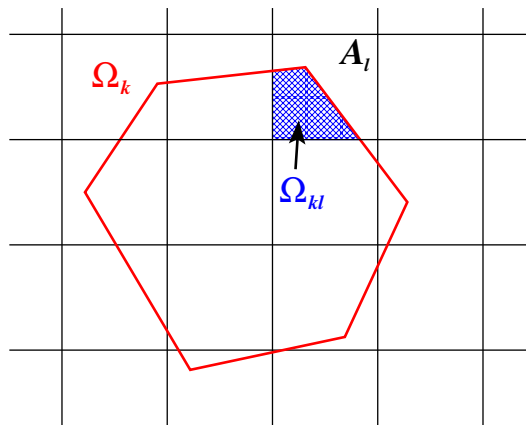


Figure 5. Schematic of the notation used to define the overlap between target grid cell Ω_k (red polygon) and high resolution cubed-sphere grid cell A_l (Cartesian-like grid on figure). The overlap area, $\Omega_{kl} = \Omega_k \cap A_l$, is shaded with cross-hatch pattern on figure.

[Title Page](#)[Abstract](#)[Introduction](#)[Conclusions](#)[References](#)[Tables](#)[Figures](#)[◀](#)[▶](#)[◀](#)[▶](#)[Back](#)[Close](#)[Full Screen / Esc](#)[Printer-friendly Version](#)[Interactive Discussion](#)

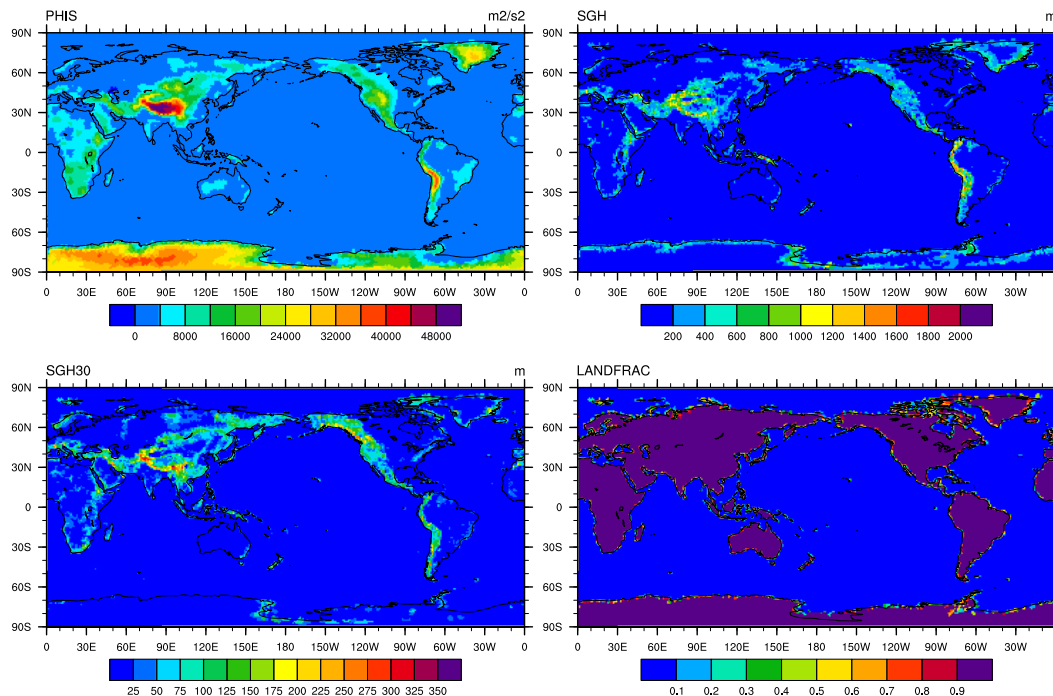


Figure 6. Surface geopotential Φ_s (upper left), *SGH* (upper right), *SGH30* (lower left) and *LANDFRAC* (lower right) for CAM-SE NE30NP4 resolution. The data is plotted on the native grid. NCL scripts to create this figure are released with the software source code.

[Title Page](#)
[Abstract](#)
[Introduction](#)
[Conclusions](#)
[References](#)
[Tables](#)
[Figures](#)
[◀](#)
[▶](#)
[◀](#)
[▶](#)
[Back](#)
[Close](#)
[Full Screen / Esc](#)
[Printer-friendly Version](#)
[Interactive Discussion](#)


[Title Page](#)
[Abstract](#)
[Introduction](#)
[Conclusions](#)
[References](#)
[Tables](#)
[Figures](#)

[Back](#)
[Close](#)
[Full Screen / Esc](#)
[Printer-friendly Version](#)
[Interactive Discussion](#)


OMEGA, JJA, model level 16 (approximately 323 hPa)

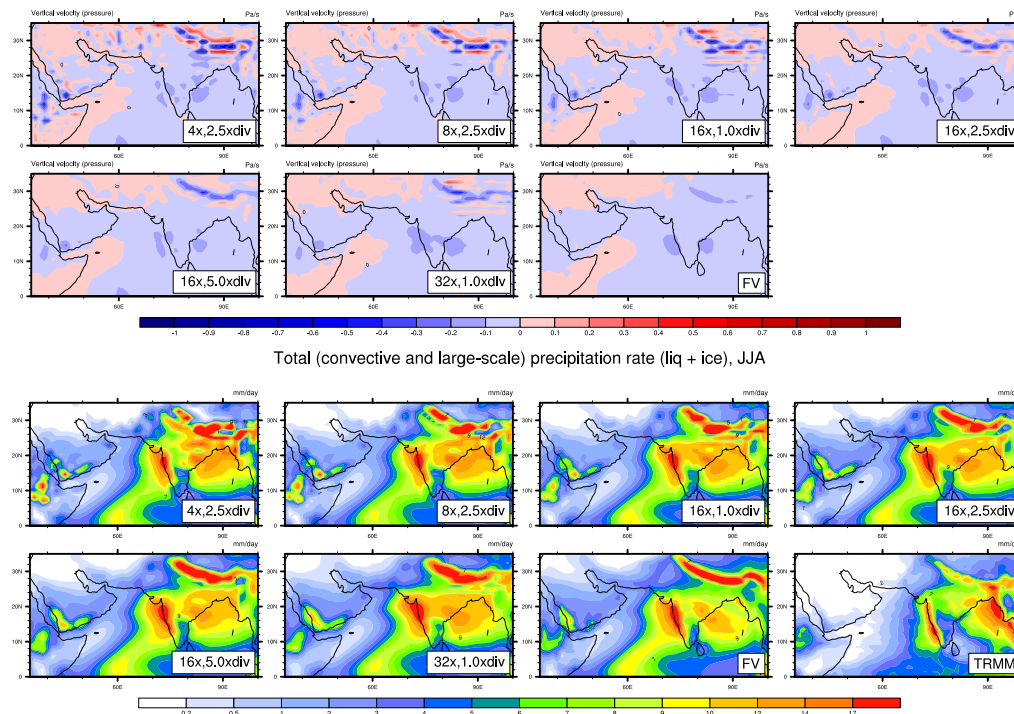


Figure 7. Diagnostics for 30 year AMIP simulations with CAM5.2. Upper and lower group of plots are model level 16 vertical velocity and total precipitation rate differences, respectively. Except for the lower right-most plot on the lower group of plots, the diagnostics are for CAM-SE with different amounts of smoothing of Φ_s and different levels of divergence damping. The amount of smoothing follows the same notation as Fig. 2 (right) and 1.0 x div, 2.5 x div, 5.0 x div refers to increasing divergence damping by a factor 1.0, 2.5^2 , and 5.0^2 , respectively. The second right-most plot on each group of plots (labeled FV) show results for CAM-FV. Lower right plot in the second group of plots show TRMM observations, respectively.

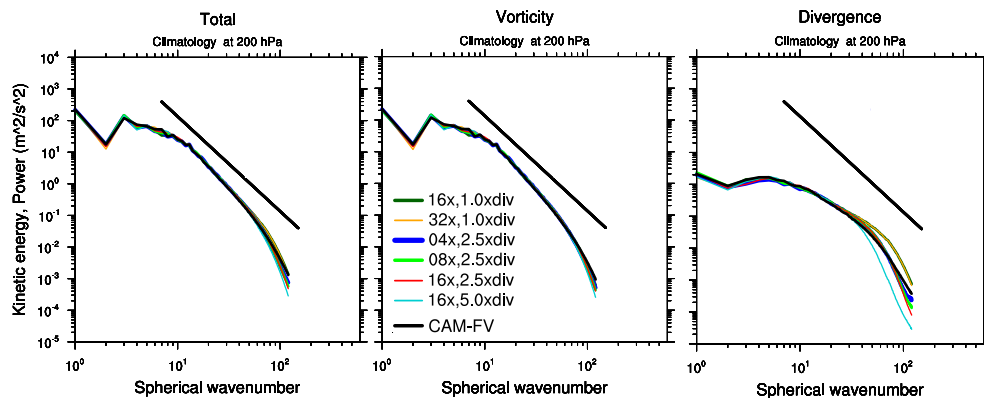


Figure 8. (left) Total kinetic energy spectrum for the velocity field at 200 hPa as a function of spherical wave number K for CAM-FV and different configurations of CAM-SE. The labeling for the CAM-SE configurations is the same as in Fig. 7. The solid-straight black line indicates the K^{-3} reference slope. The middle and right plots show the kinetic energy partitioned into divergent and rotational modes, respectively. The spectra have been computed using daily instantaneous wind and surface pressure data for a 2 month period.

[Title Page](#)
[Abstract](#)
[Introduction](#)
[Conclusions](#)
[References](#)
[Tables](#)
[Figures](#)
[⏪](#)
[⏩](#)
[◀](#)
[▶](#)
[Back](#)
[Close](#)
[Full Screen / Esc](#)
[Printer-friendly Version](#)
[Interactive Discussion](#)
